Supporting Information

Carbon-coated WS_2 Nanosheets Supported on Carbon Nanofibers for High-rate Potassium-ion Capacitors

Shitao Geng,[a] Tong Zhou,*[a] Minyu Jia,[a] Xiangyan Shen,[b] Peibo Gao,[a] Shuang Tian,[a] Pengfei Zhou,[b] Bo Liu,[a] Jin Zhou,*[b] Shuping Zhuo,[b] and Feng Li*[c]

[a] School of Physics and Optoelectronic Engineering, Shandong University of Technology, Zibo 255049, China

E-mails: zhoutong@sdut.edu.cn

[b] School of Chemistry and Chemical Engineering, Shandong University of Technology, Zibo 255049, China

E-mails: zhoujin@sdut.edu.cn

[c] Shenyang National Laboratory for Materials Science, Institute of Metal Research, Chinese Academy of Sciences, Shenyang 110016, China

E-mail: fli@imr.ac.cn

Experiment Section

***Preparation of CNFs*:** Typically, 11.2 g of polyacrylonitrile (PAN, M_w = 150 000, Sigma-Aldrich Co., Ltd.) was added into 20 mL of N, N-dimethylformamide (DMF, 99.5%, Sinopharm Chemical Reagent Co., Ltd). The mixture was stirred for 12 h at room temperature until the solution became transparent. 10 mL stainless steel syringe (inner diameter 0.71 mm) was used to load the precursor solution. In the electrospinning process, the flow rate was controlled at about 0.05 mL h^{-1}, and the indoor humidity was controlled below 25%. The electrospun nanofibers drew out under electrostatic field originating from 16 kV of positive voltage on the needle and 3 kV of negative voltage on the aluminum foil collector. Afterward, the pre-oxidized PAN nanofiber was obtained by heating to 260 ℃ for 2 h. Finally, the CNFs membrane was prepared via carbonization at 800 ℃ for 2 h in tube furnace under Ar atmosphere.

***Preparation of O-WS$_2$@CNFs*:** 120 mg of ammonium tungsten sulfide ($(NH_4)_2WS_4$, ≥ 99.9%, Sigma-Aldrich Co., Ltd.) was dissolved in 35 mL of DMF. The green reaction solution and 0.3 mg of CNFs (area of 900 mm^2) were transferred to Teflon-lined autoclave and heated at 200 ℃ for 16 h. The product was washed repetitiously with deionized water and ethanol. Finally, the O-WS_2@CNFs was obtained after dried at 60 ℃ overnight.

***Preparation of WS$_2$@CNFs*:** The O-WS_2@CNFs and sulfur powder (≥ 99.95%, Sigma-Aldrich Co., Ltd.) was placed in the middle and the upstream part of the tube furnace, respectively. Ar with the flow rate of 20 sccm was continuous throughout the whole process of vulcanization. The tube furnace was heated to 800 ℃ at heating rate

of 5 °C min^{-1} and maintained at 800 °C for 2 h. After cooled back to room temperature, the WS_2@CNFs was finally obtained.

***Preparation of C-WS_2@CNFs*:** The WS_2@CNFs was immersed in 100 mL of Tris-buffered solution (10 mM, pH 8.5). 200 mg of dopamine (98%, Aladdin Co., Ltd.) was added to the solution with stirring for 5 h to obtain the PDA-coating WS_2@CNFs. Afterward, the composite was washed several times with deionized water, followed by drying for 12 h at 60 ℃. Finally, the C-WS_2@CNFs was carbonized in tube furnace under Ar atmosphere at 550 ℃ for 3.5 h to obtain the C-WS_2@CNFs.

***Preparation of ACNFs*:** First, the CNFs were immersed in 4.0 M KOH solution and evacuated for 20 min to ensure that the KOH solution was able to infiltrate the CNFs fully, and continue to soak for 24 h in air atmosphere. After taking it out, it was dried at 80 °C for 2 h. The obtained product of KOH/CNFs was placed in tube furnace for activation treatment. The furnace temperature was heated up to 800 °C for 2 h with heating rate of 5 °C min^{-1}. The obtained product was washed with 1.0 M HCl solution, followed by washing with a large amount of de-ionized water, and finally dried at 80 °C for 12 h to obtain ACNFs.

***Material Characteristics*:** SEM and TEM images of samples were taken by field emission scanning electron microscope (FESEM, HITACHI, SU8010) and transmission electron microscope (TEM, FEI Tecnai G2 F20 S-TWIN). X-ray powder diffraction (XRD) patterns were recorded from Bruker D8 Advance powder X-ray diffractometer with Cu Ka (λ = 0.15406 nm). Raman spectra were collected from a LabRAM HR evolution spectrometer under the excitation of 532 nm laser. For the *in*

situ Raman test, the ECC-Opto-Std test cell (EL-Cell GmbH) was used for the assembly of the K half cell. BET surface area and pore size distribution were evaluated by N_2 adsorption/desorption analyzer (ASAP 2420, Micrometrics). X-ray photoelectron spectroscopy was measured by X-ray photoelectron spectroscopy (XPS, Thermo ESCALAB 250Xl). Thermogravimetric analysis (TGA) was performed using Perkin-Elmer TGA 4000 at rate of 5 ℃ min^{-1} at 30-800 ℃.

***Electrochemical Measurement*:** The as-prepared O-WS_2@CNFs, WS_2@CNFs, and C-WS_2@CNFs membranes were cut into identical pieces and used directly as the working electrodes. All electrodes with an areal density of about 1.0 mg cm^{-2} were assembled into CR2032-type cells under Ar glove box (H_2O and O_2 < 0.01 ppm, Mbraun, Unilab). K foil was used as the anode and 1.0 M KFSI in EC: DMC = 1:1 vol% was used as the electrolyte. Galvanostatic charge/discharge tests were performed with the Land CT2001A battery testing system. Cyclic voltammetry and electrochemical impedance spectroscopy were carried out on an electrochemical workstation (IVIUM technology, nSTAT). The current density and the capacity are based on the total mass of the electrodes.

***GITT Measurement*:** Measurements of GITT profiles were made with pulse current at 0.05 A g^{-1} for 30 min between rest intervals for 1 h. The diffusivity coefficient can be estimated according to Fick's second law as follows:

$$D_k^+ = \frac{4}{\pi\tau}\left(\frac{m_B V_M}{M_B S}\right)^2\left(\frac{\Delta E_S}{\Delta E_t}\right)^2$$

where m_B and M_B are the effective mass and molar mass of the electrode material, respectively. V_M is the molar volume, S is the surface area of the electrode; ΔE_S is the

voltage change between the initial and steady state, ΔE_t is the constant current discharge/charge potential change.

***DFT Calculation Method*:** First-principle calculations were performed by the density functional theory (DFT) using the Vienna Ab-initio Simulation Package (VASP) package [*Comput. Mater. Sci.* 1996, 6, 15-50]. The generalized gradient approximation (GGA) with the Perdew- Burke-Ernzerhof (PBE) functional was used to describe the electronic exchange and correlation effects [*Phys. Rev. Lett.* 1996, 77, 3865-3868]. Uniform G-centered k-points meshes with a resolution of 2π*0.03 $Å^{-1}$ and Methfessel-Paxton electronic smearing were adopted for the integration in the Brillouin zone for geometric optimization. The simulation was run with cutoff energy of 500 eV throughout the computations. These settings ensure convergence of the total energies to within 1 meV per atom. Structure relaxation proceeded until all forces on atoms were less than 1 meV $Å^{-1}$ and the total stress tensor was within 0.01 GPa of the target value. The climbing-image nudged elastic band (cNEB) method [*J. Chem. Phys.* 2000, 113, 9901] implemented in VASP was performed to investigate the transition state searches.

***Fabrication of PIC full cell*:** PIC devices were also assembled in 2032 coin-type cells. Before assembling the PIC full cell, the C-WS_2@CNFs anode was pre-cycled five times at 0.05 A g^{-1} in half cell. PICs full cell was assembled by the pre-activated C-WS_2@CNFs and ACNFs with mass ratios of 1:1, 1:2 and 1:3.

In PIC full-cell tests, the specific capacities and current densities were all based on the total mass of both anode and cathode materials. The calculations of energy density (E, Wh kg^{-1}) and power densities (P, W kg^{-1}) were performed using the equations

below:

$$E = \int_{t_1}^{t_2} IVdt = \Delta V \times \frac{I}{m} \times t \qquad P = \frac{E}{t}$$

where ΔV represents the potential change after full discharge, I is the constant discharge current, and m is the total mass of the anode and cathode materials, t is the time for a full discharge.

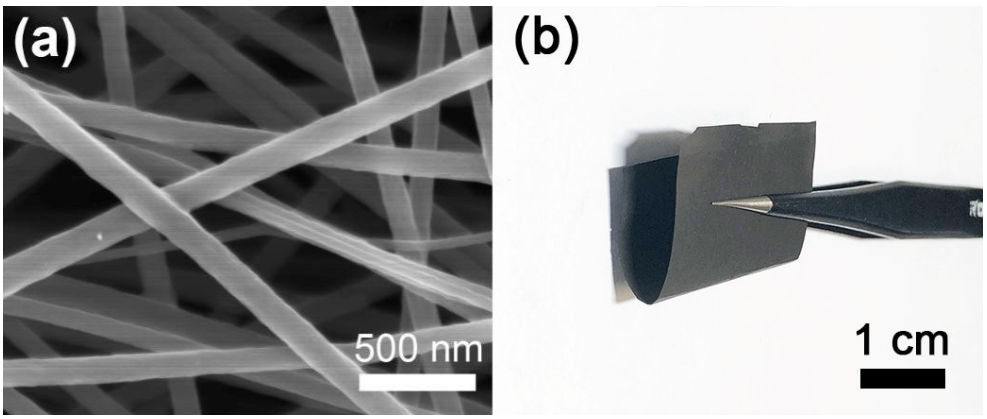

Fig. S1 (a) SEM image and (b) photograph of the CNFs membrane.

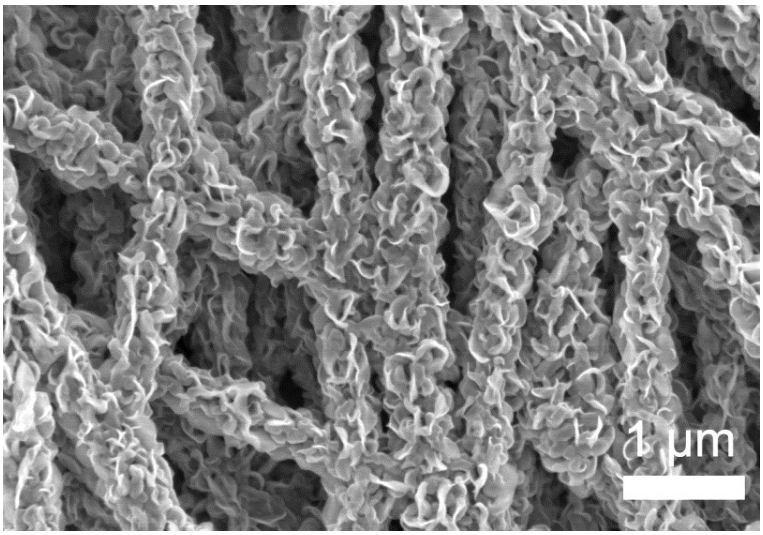

Fig. S2 SEM image of the O-WS_2@CNFs.

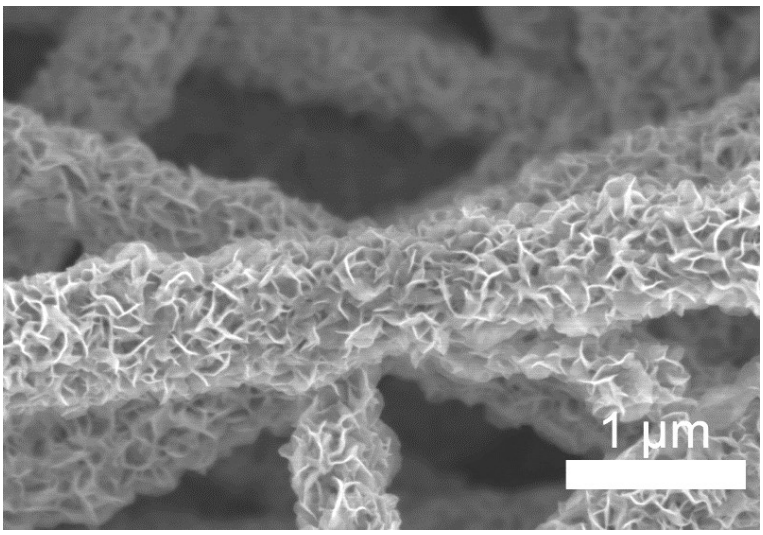

Fig. S3 SEM image of the WS_2@CNFs.

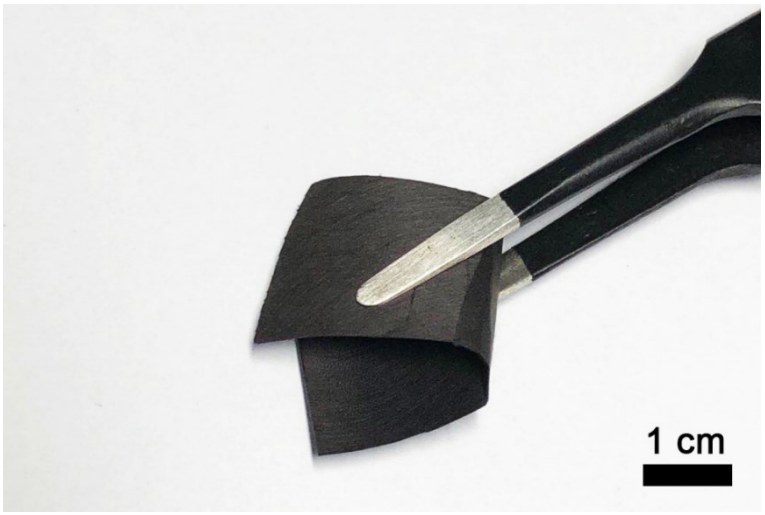

Fig. S4 Photograph of the folded C-WS_2@CNFs.

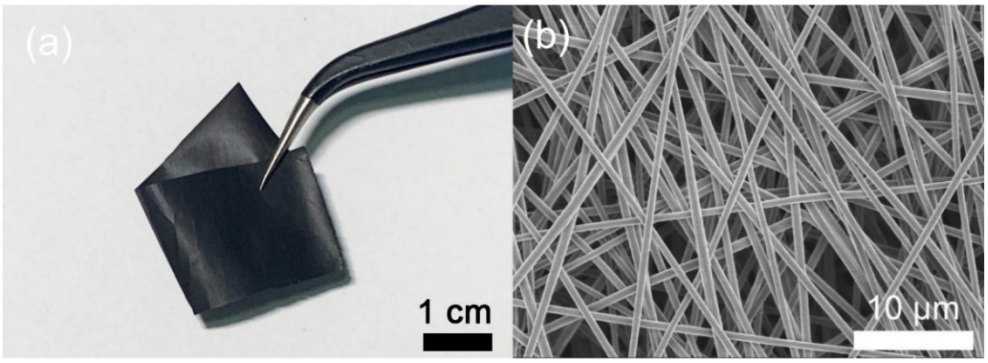

Fig. S5 (a) Photograph of the folded ACNFs, and (b) SEM image of the ACNFs.

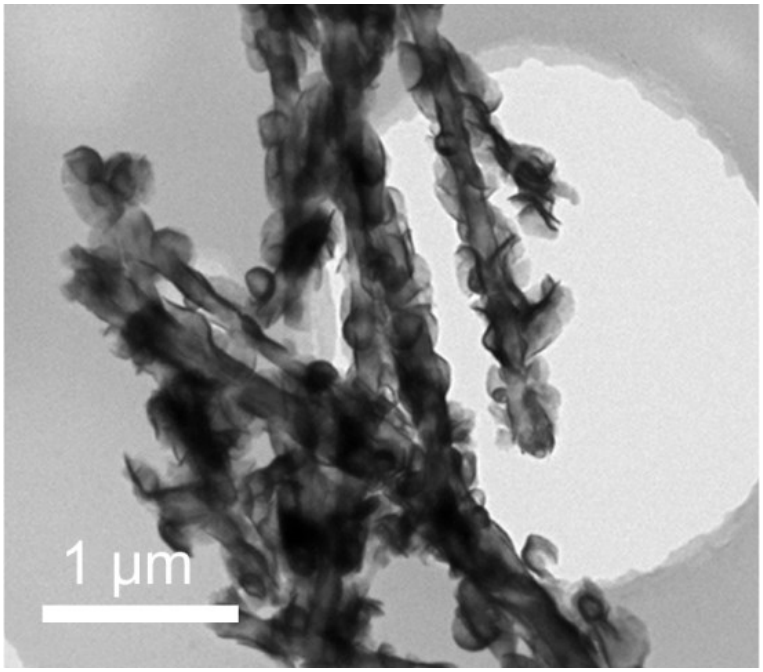

Fig. S6 TEM image of the C-WS_2@CNFs.

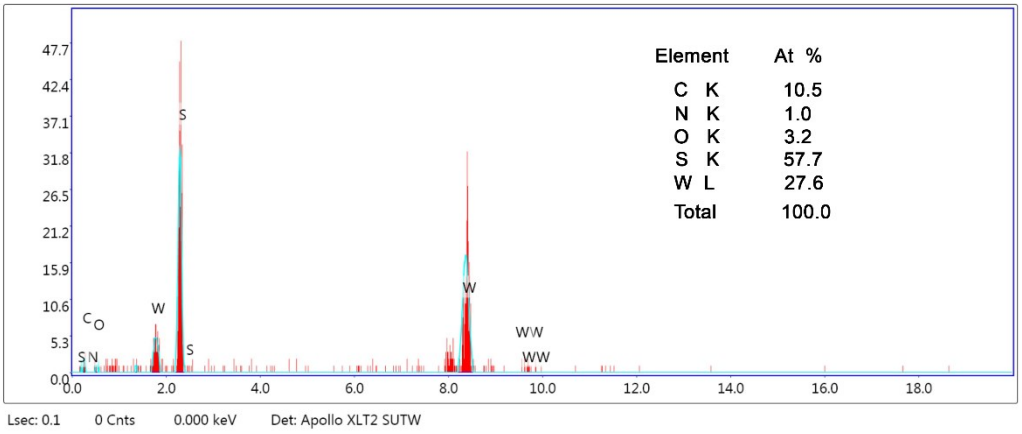

Fig. S7 EDS spectrum of the WS_2@CNFs.

Table S1 Element compositions of the samples by XPS

Element (at%) / Sample	W	S	C	N	O
C-WS_2@CNFs	6.59	14.06	59.77	6.64	12.94
WS_2@CNFs	30.39	61.94	2.02	2.03	3.62
O-WS_2@CNFs	11.70	13.78	27.70	7.55	39.27

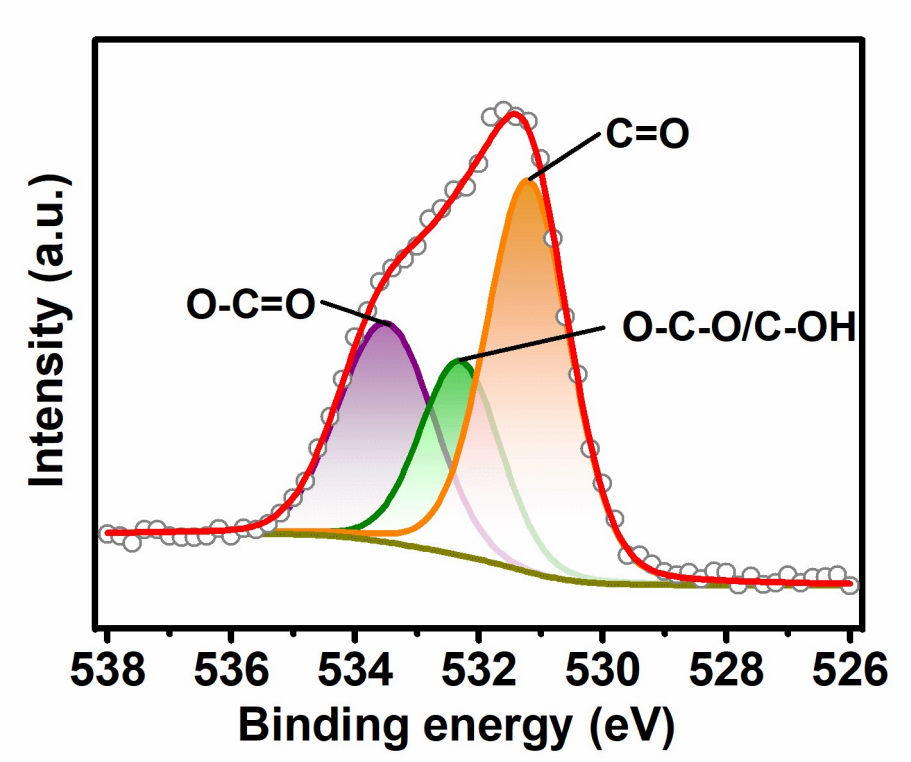

Fig. S8 The O 1s spectrum of C-WS_2@CNFs

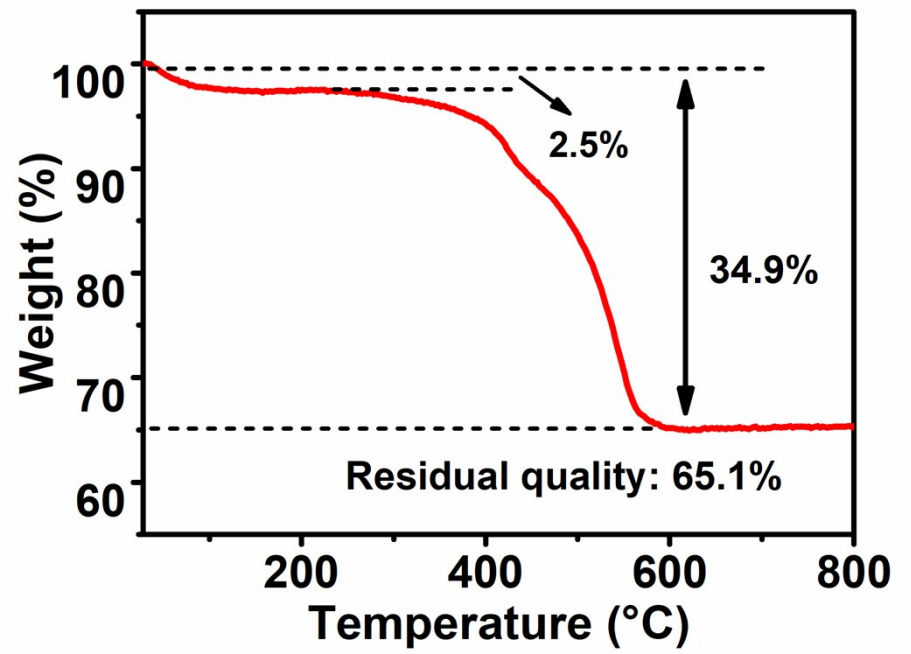

Fig. S9 TGA of C-WS_2@CNFs.

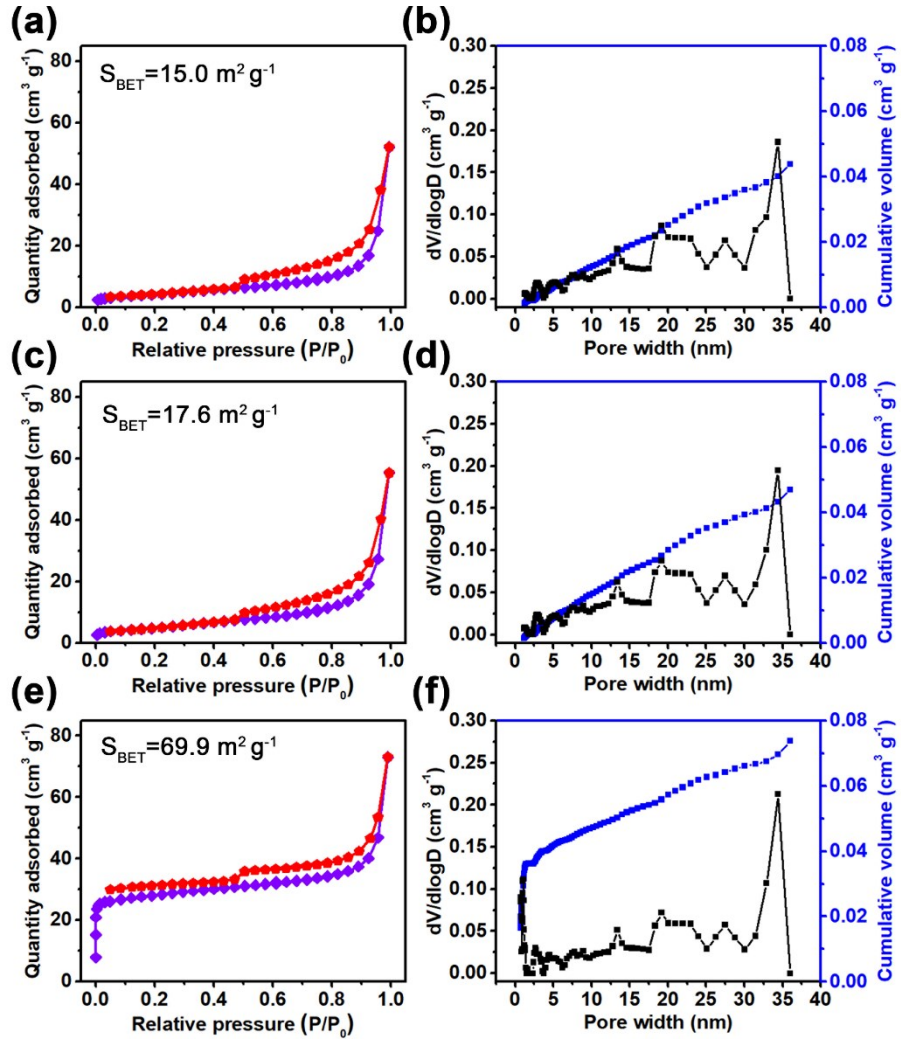

Fig. S10 (a) N_2 adsorption-desorption isotherm, and (b) pore size distribution of the C-WS_2@CNFs.

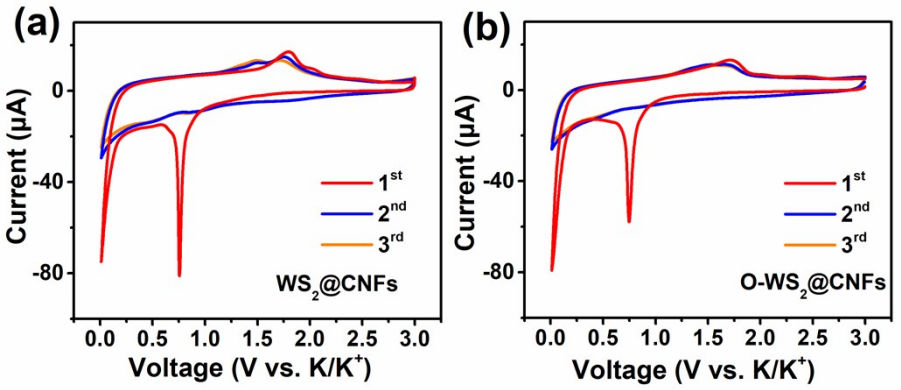

Fig. S11 The initial three CV curves at 0.2 mV s^{-1} of (a) WS_2@CNFs, (b) O-WS_2@CNFs.

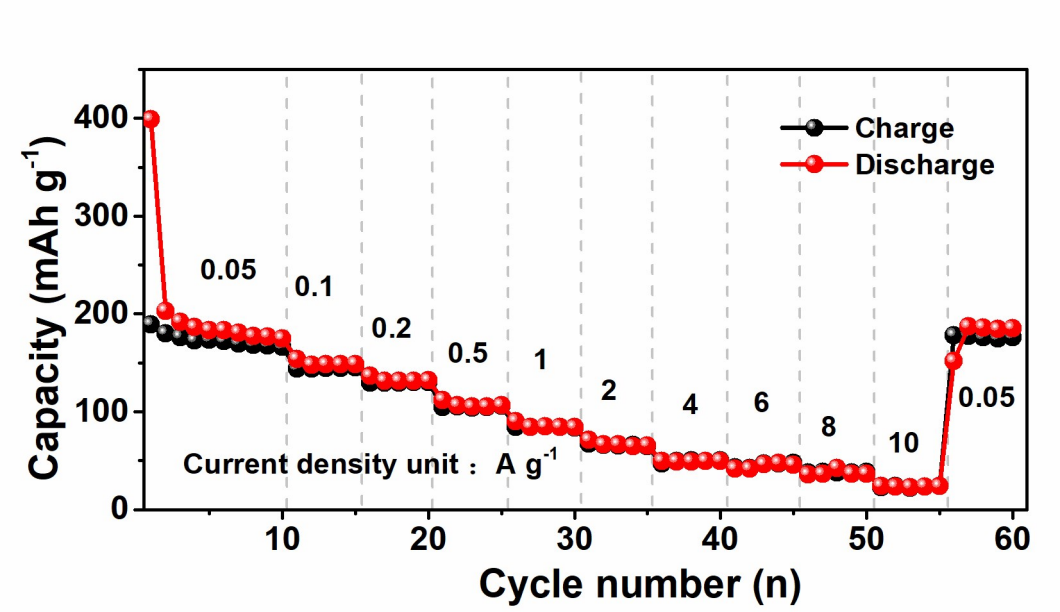

Fig. S12 Rate capabilities of the CNFs.

Table S2 Comparison of the initial Coulombic efficiency of C-WS_2@CNFs anode with previously reported anode materials for PIBs.

Anode materials	Current	Initial Coulombic	Reference
C-WS_2@CNFs	**0.05**	**68.6%**	**This work**
ED-MoS_2	0.1	40.9%	Adv. Funct. Mater. **2020**, 1908755
C/$MoSe_2$/MXene	0.2	54.2%	ACS Nano **2019**, 13, 3448−3456
$FeSe_2$/N-C	0.1	37%	Adv. Energy Mater. **2019**, 1903277
$NbSe_2$/NSeCNFs	0.05	56.7%	Adv. Funct. Mater. **2020**, 2004247
SnO_2 Nanoparticles	0.02	43.3%	Energy Environ. Sci., **2020**, 13, 571−578
N-doped Hollow Carbon	0.1	16.3%	Energy Environ. Sci., **2019**, 12, 1605−1612
Sulfur-Grafted Hollow Carbon	0.025	51.4%	Adv. Mater. **2019**, 1900429
WS_2@NCNs	0.05	48.8%	Matter **2019**, 1, 893−910

Table S3 Comparison of the electrochemical performance of C-WS_2@CNFs anode with previously reported anode materials for PIBs.

Anode materials	Rate capability	Reference
C-WS_2@CNFs	**319 mAh g^{-1}@0.05 A g^{-1}** **234 mAh g^{-1}@ 1 A g^{-1}** **219 mAh g^{-1}@2 A g^{-1}** **168 mAh g^{-1}@10 A g^{-1}**	**This work**
V_2O_3@PNCNFs	245 mAh g^{-1}@0.05 A g^{-1} 138 mAh g^{-1}@1 A g^{-1}	Nano Energy **2018**, 50, 462-467
VSe_2 NSs	374 mAh g^{-1}@0.1 A g^{-1} 180 mAh g^{-1}@1 A g^{-1}	Adv. Mater. **2018**, 1800036
S-HCS	389 mAh g^{-1}@0.1 A g^{-1} 108 mAh g^{-1}@ 5A g^{-1}	Adv. Mater. **2019**, 1900429
$MoSe_2$/N-C	303 mAh g^{-1}@0.1 A g^{-1} 178 mAh g^{-1}@2 A g^{-1}	Adv. Energy Mater. **2018**, 1801477
MoS_2@rGO	399 mAh g^{-1}@0.1 A g^{-1} 195 mAh g^{-1}@2 A g^{-1}	Nano Energy **2019**, 63, 103868
$NbSe_2$/rGO	281 mAh g^{-1}@0.05 A g^{-1} 81 mAh g^{-1}@2A g^{-1}	Adv. Funct. Mater. **2020**, 2004247
VS_2 NSA	412 mAh g^{-1}@0.1A g^{-1} 101 mAh g^{-1}@2A g^{-1}	Adv. Mater. **2017**, 1702061
$FeSe_2$/N-C	291 mAh g^{-1}@0.1 A g^{-1} 151 mAh g^{-1}@ 2A g^{-1}	Adv. Energy Mater. **2019**, 1903277
WS_2 powder	115 mAh g^{-1}@0.05 A g^{-1} 62 mAh g^{-1}@0.8 A g^{-1}	Nano Res. **2019**, 1998-0124
WS_2@NCNs	415 mAh g^{-1}@0.05 A g^{-1} 198 mAh g^{-1}@1A g^{-1}	Matter **2019**, 1, 893−910

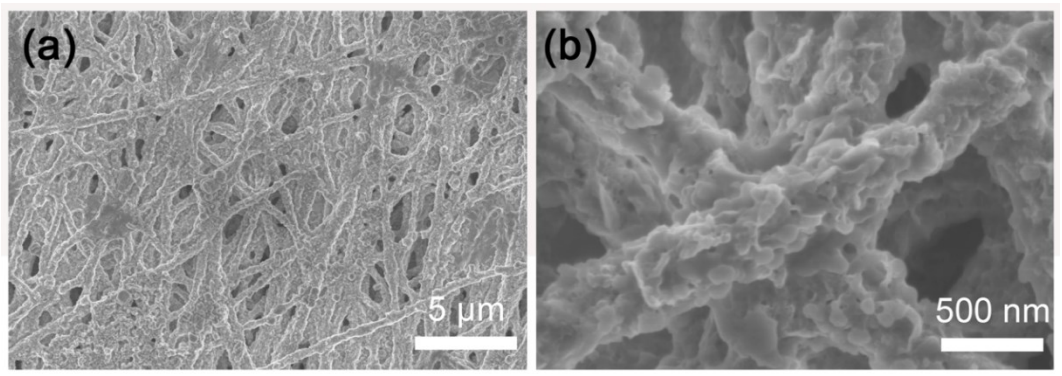

Fig. S13 (a, b) SEM of the C-WS_2@CNFs electrode after the 300 cycles.

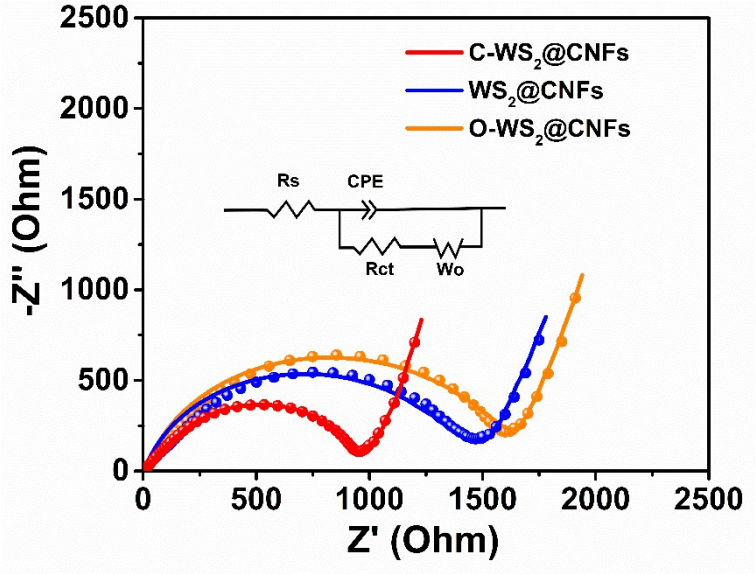

Fig. S14 Electrochemical impedance spectroscopy (EIS) and the data fitting results of C-WS_2@CNFs, WS_2@CNFs, and O-WS_2@CNFs. The inset shows the corresponding equivalent circuit used for the data fitting, where R_s, R_{ct}, CPE, and W_O represent contact resistance, charge-transfer resistance, constant-phase element, and Warburg ion-diffusion resistance, respectively.

Table S4 The resistor elements of three samples derived from the Nyquist plots.

Sample	R_s (Ω)	R_{ct} (Ω)	W_O (Ω)
C-WS_2@CNFs	3.9	917	169
WS_2@CNFs	5.3	1361	451
O-WS_2@CNFs	5.2	1567	183

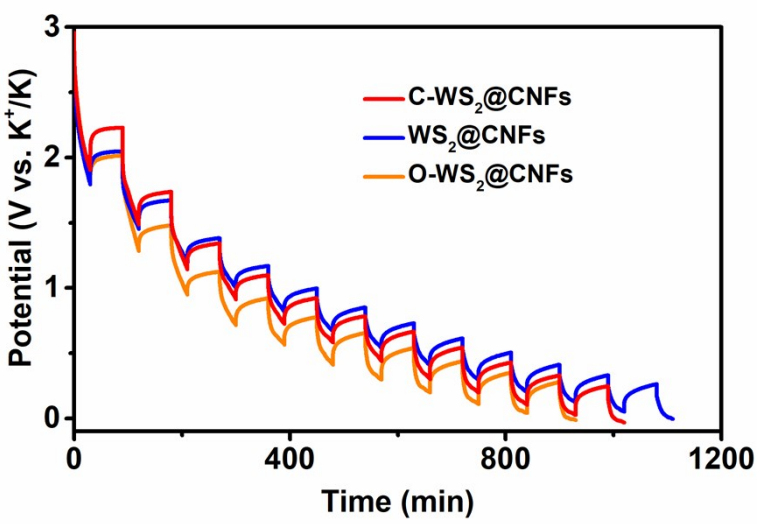

Fig. S15 GITT profiles of the discharging process of the three electrodes.

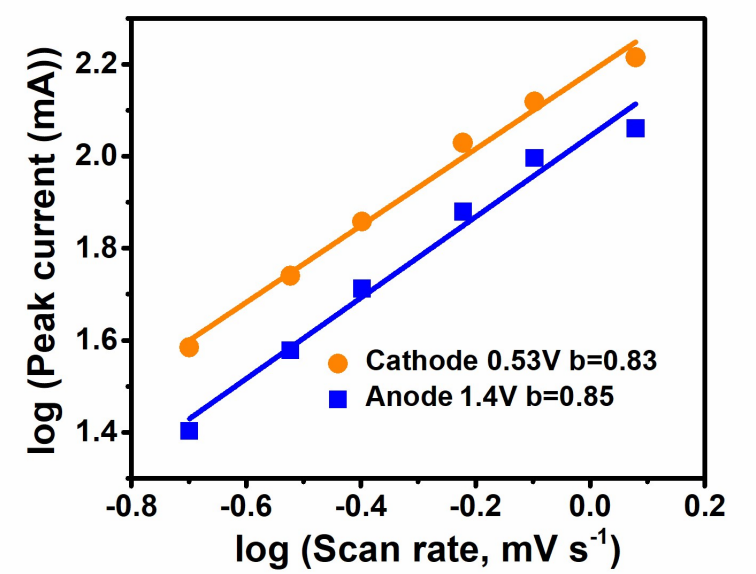

Fig. S16 Determination of the b-value according to the relationship between peak current and scan rate.

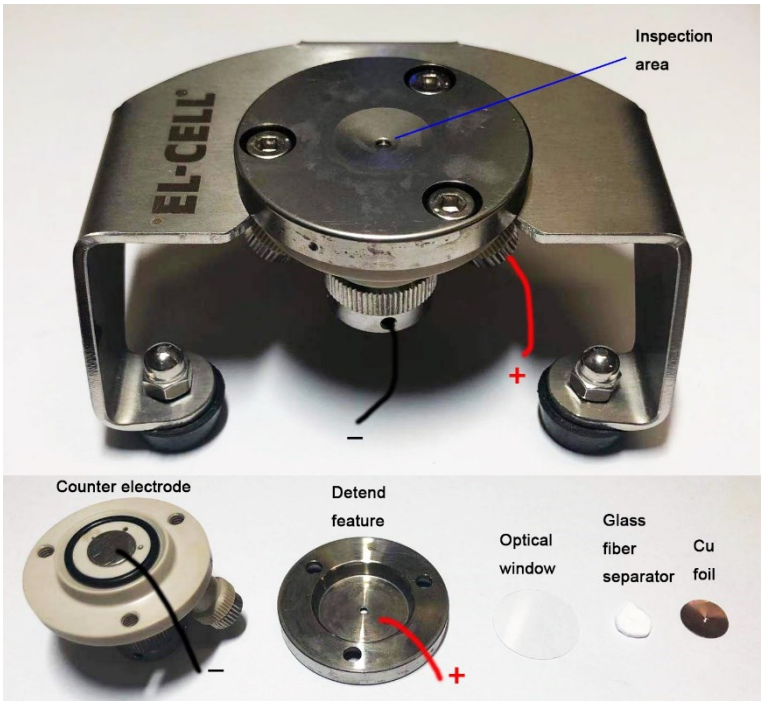

Fig. S17 The ECC-Opto-Std test cell and its parts for the *in situ* Raman spetra testing.

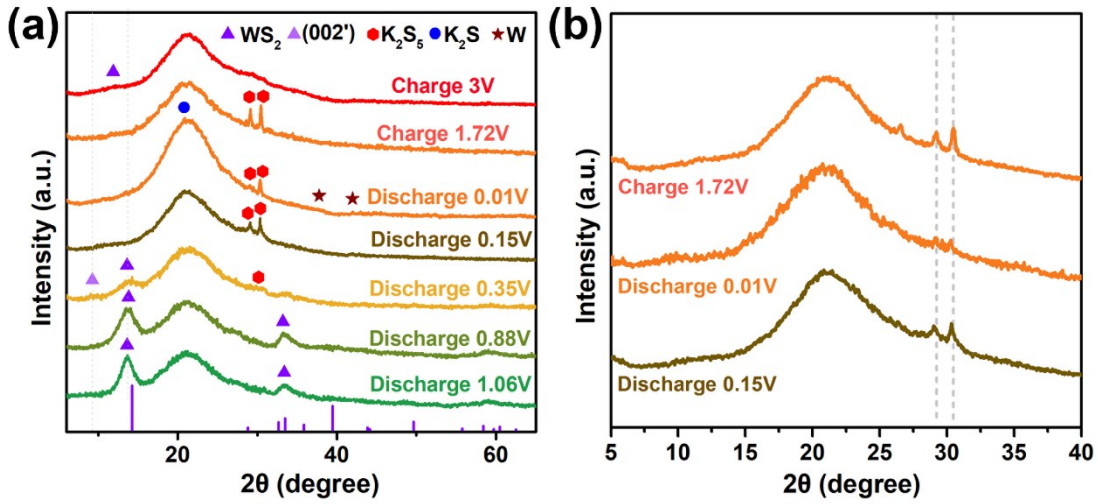

Fig. S18 (a) *Ex situ* XRD patterns of C-WS_2@CNFs (a) the 1st discharge-charge process, (b) the 3rd discharge-charge process

The phase transition of C-WS_2@CNFs was further identified by *ex situ* XRD at different discharge/charge states (Fig. S18). When the C-WS_2@CNFs electrode is

discharged from 1.04 to 0.88 V, the peaks of the pristine WS_2 are still found and remained essentially unchanged. Upon further potassiation at 0.35 V, the predominant (002) Bragg peak at 14.1° weakens, while a new peak named (002') is collected at 9.8° corresponding to enlarged interlayer space of 0.790 nm. These changes further confirm the formation of K^+-intercalated WS_2 (K_xWS_2). After the electrode is discharged to 0.15 V, the intermediate phase of K_2S_5 (JCPDS No. 30-0993) is identified, demonstrating the continuation of the conversion reactions. As the potassiation continues to 0.01 V, the K_2S_5 signal gradually fades, accompanied by the appearance of a peak at 20.84° corresponding to the (111) plane of cubic K_2S (JCPDS No. 74-1030). Two small peaks appear around 37.7° and 42.0°, which are indexed to the (111) and (200) planes of W (JCPDS No. 88-2339). Upon depotassiation at 1.72 V, the peak of the K_2S_5 phase reappears. When fully charged to 0.01 V, a faint WS_2 peak with slight shift compared to that of pristine WS_2 is detected, indicating the irreversible structural degradation of WS_2 caused by the phase conversion during the charge/discharge cycle. This intermediate phase of K_2S_5 could be also identified by the ex situ XRD measurement for the 3rd discharge/charge cycle (Fig. S18b). In detail, the intermediate phase of K_2S_5 can be determined when the electrode is discharged to 0.15 V according to the two diffraction peaks at 2θ= 29.1° and 30.4° (JCPDS No. 30-0993). These peaks significantly became weak when it was further discharge to 0.01 V, and reappeared when it was re-charged to 1.72 V. These results further confirm the well reproducibility of the intermediate phase of K_2S_5 and the conversion reaction mechanism between K^+ and WS_2.

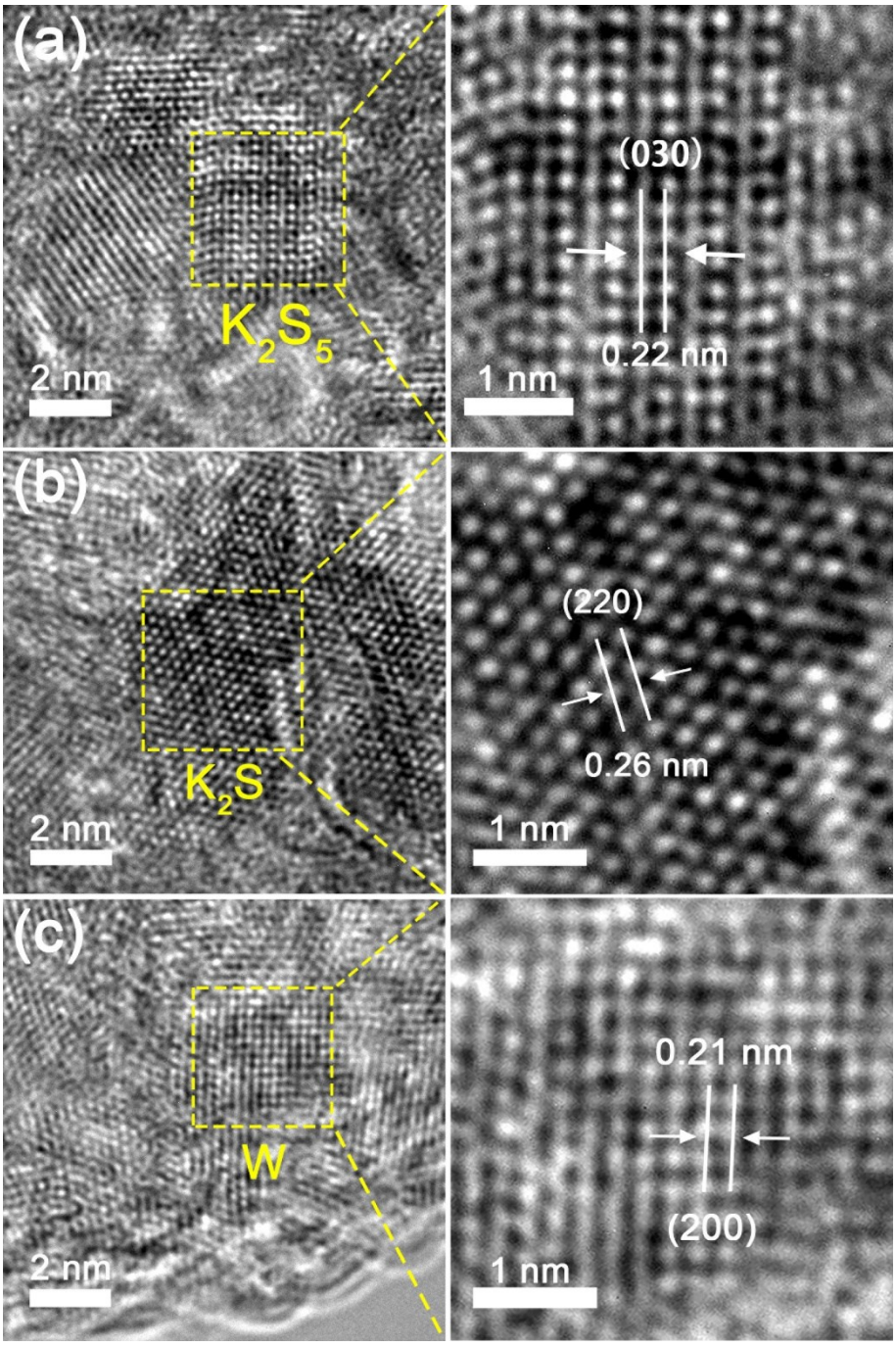

Fig. S19 *Ex situ* HRTEM images of C-WS_2@CNFs at discharged to 0.01 V: (a) K_2S_5, (b) K_2S, and (c) W.

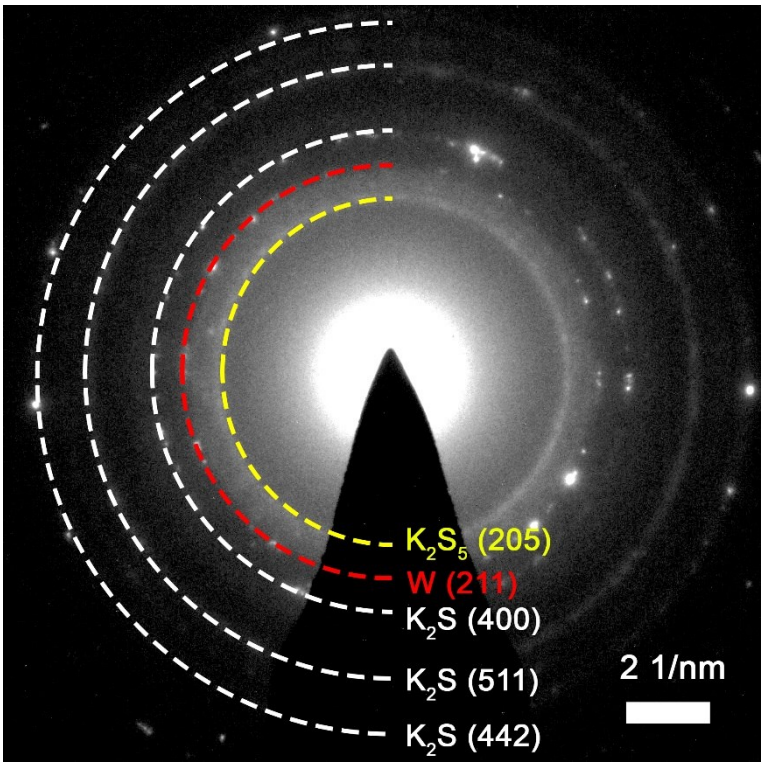

Fig. S20 SAED pattern of the discharged C-WS_2@CNFs electrode.

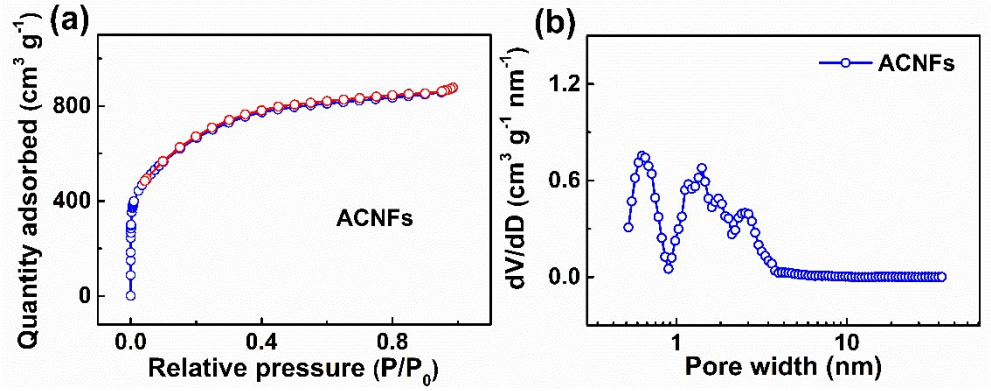

Fig. S21 (a) Nitrogen adsorption-desorption isothermal curves and b) pore size distribution of ACNFs.

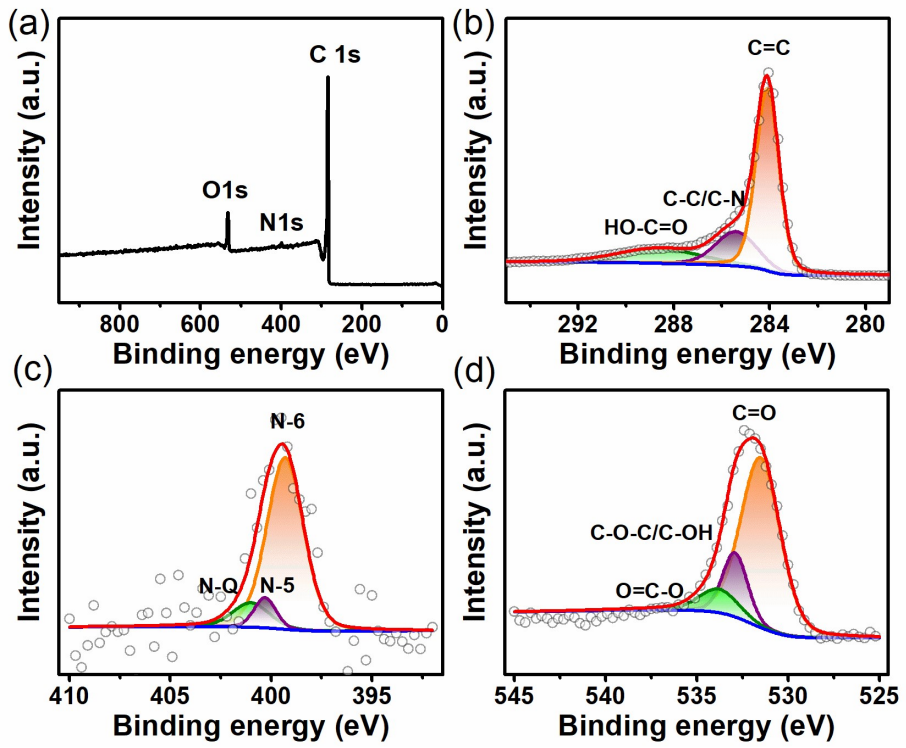

Fig. S22 (a) XPS survey, high-resolution XPS spectra of (b) C1s, (c) N1s, and (d) O1s of ACNFs.

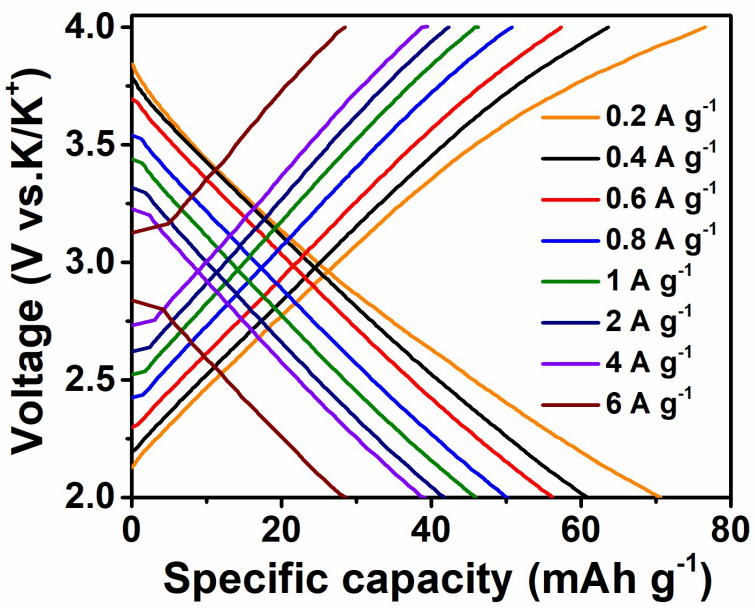

Fig. S23 Charge/discharge plots at different current densities of ACNFs.

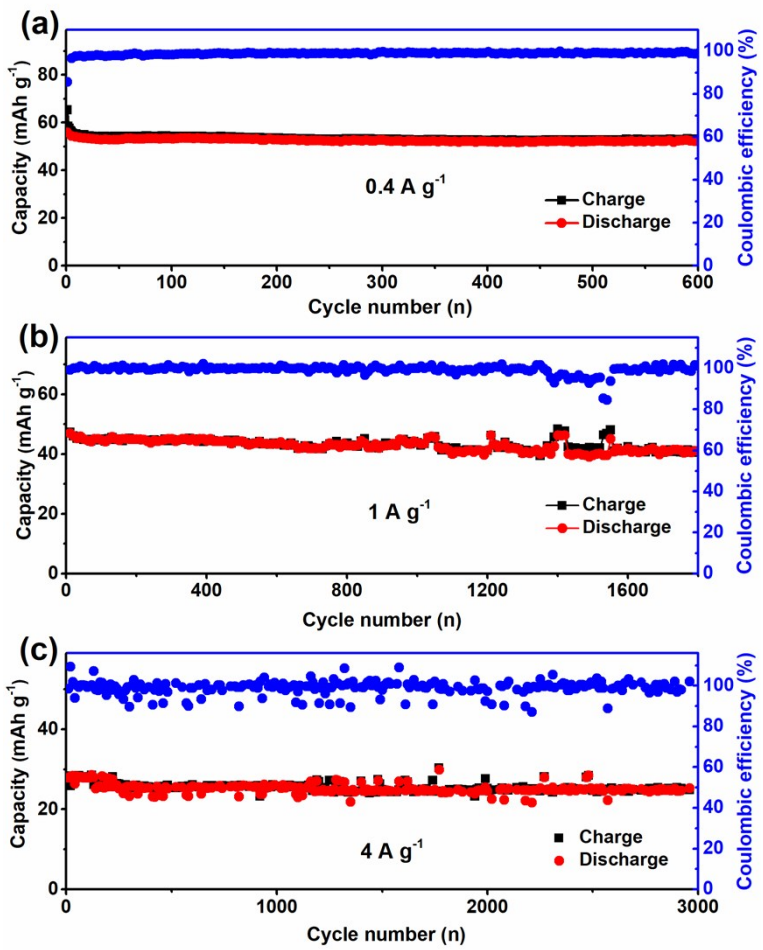

Fig. S24 Cycle performance of ACNFs at different current densities.

Table S5 Comparison of the C-WS_2@CNFs||ACNFs with previously reported PICs.

PICs	Rate capability	Reference
C-WS_2@CNFs||ACNFs	**180.4 Wh kg^{-1} @399.6 W kg^{-1} 42 Wh kg^{-1}@12.6 kW kg^{-1}**	**This work**
S-N-PCNs||AC	170.3 Wh kg^{-1}@196.7 W kg^{-1} 79.8 Wh kg^{-1}@ 5.4 kW kg^{-1}	Adv. Energy Mater. **2019**, 1901533
$NbSe_2$/NSeCNFs||AC	136.2 Wh kg^{-1}@182.0 W kg^{-1} 18.6 Wh kg^{-1}@ 4.1 kW kg^{-1}	Adv. Funct. Mater. **2020**, 2004247
$FeSe_2$/N-C||AC	232.2 Wh kg^{-1}@198.1W kg^{-1} 29.9Wh kg^{-1}@ 7.5 kW kg^{-1}	Adv. Energy Mater. **2019**, 1903277
CTP||AC	76.2 Wh kg^{-1}@126.3 W kg^{-1} 47.0 Wh kg^{-1}@ 1.8 kW kg^{-1}	Adv. Funct. Mater. **2018**, 1802684
NHCS||ANHCS	109.5 Wh kg^{-1}@189.2 W kg^{-1} 18.4 Wh kg^{-1}@ 8.3 kW kg^{-1}	Adv. Funct. Mater. **2019**, 1903496
N-$MoSe_2$/G||AC	103.0 Wh kg^{-1}@209.9 W kg^{-1} 31.2 Wh kg^{-1}@ 6.8 kW kg^{-1}	Adv. Funct. Mater. **2019**, 1903878
K_2TP||AC	84.0 Wh kg^{-1}@209.9 W kg^{-1} 51.2 Wh kg^{-1}@ 2.0 kW kg^{-1}	Chem. Sci., **2019**, 10, 2048
Soft carbon||AC	92.6 Wh kg^{-1}@197.0 W kg^{-1} 13.8 Wh kg^{-1}@ 0.6 kW kg^{-1}	Adv. Mater. **2018**, 1800804
3D-Ti_3C_2||HPAC	98.4 Wh kg^{-1}@120.8 W kg^{-1} 18.7 Wh kg^{-1}@ 7.0 kW kg^{-1}	Adv. Funct. Mater. **2020**, 2005663
MDPC||PDPC	120.0 Wh kg^{-1}@260 W kg^{-1} 21.7 Wh kg^{-1}@ 26 kW kg^{-1}	Adv. Funct. Mater. **2020**, 2006561
S-MCCF||aMCCF	100 Wh kg^{-1}@200 W kg^{-1} 58.3 Wh kg^{-1}@ 10 kW kg^{-1}	Nano-Micro Lett. **2021**, 13:14
WS_2@NCNs||NCHS	103.7 Wh kg^{-1}@235.5 W kg^{-1} 66.4 Wh kg^{-1}@ 2.3 kW kg^{-1}	Matter **2019**, 1, 893−910